ACS OMEGA

Open Access

http://pubs.acs.org/journal/acsodf

Article

Improving Interfacial Stability for All-Solid-State Secondary Batteries with Precursor-Based Gradient Doping

Yong Jun Ji and Yong Joon Park*

Cite This: *ACS Omega* 2024, 9, 8405−8416

Read Online

ACCESS | Metrics & More | Article Recommendations | Supporting Information

ABSTRACT: Recently, sulfide solid-state electrolytes with excellent ionic conductivity and facile electrode integration have gained prominence in the field of all-solid-state batteries (ASSBs). However, owing to their inherently high reactivity, sulfide electrolytes interact with the cathode, forming interfacial layers that adversely affect the electrochemical performance of all-solid-state cells. Unlike conventional cathode-coating methods that involve the formation of surface coatings from high-cost source materials, the proposed strategy involves the doping of precursors with low-cost oxides (Nb_2O_5, Ta_2O_5, and La_2O_3) prior to cathode fabrication. This novel approach aims to improve the stability of the cathode−sulfide electrolyte interface. Notably, doping significantly improved the discharge capacity, rate capability, and cyclic performance of cathodes while reducing their impedance resistance. Scanning electron microscopy, transmission electron microscopy (TEM), and X-ray photoelectron spectroscopy (XPS) indicated a gradient dopant−concentration profile (with a high level of dopant at the surface) in the doped cathodes. Cathode doping, particularly with Nb and Ta, caused a reduction in cation mixing owing to crystal-structure adjustments and ionic-conductivity enhancements. XPS and high-resolution TEM confirmed that gradient doping effectively minimized cathodic side reactions, possibly due to the formation of a coating-like protective layer in the cathode−electrolyte interface coupled with structural stabilization attributed to the doping process. The protective ability of the interfacial layer generated by gradient doping was confirmed to be comparable to that of conventional surface coatings. Therefore, this study could guide the future development of low-cost, high-performance ASSBs, opening new frontiers in sustainable energy storage.

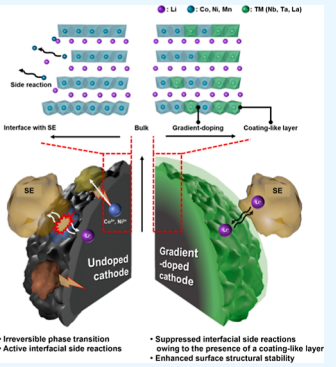

INTRODUCTION

In recent years, the adoption of Li-ion secondary batteries (LIBs) in electric vehicles and energy storage systems has rapidly increased in scale and prominence,[1−7] resulting in a significant increase in the concomitant safety concerns. Human casualties owing to battery explosions and fires have limited the widespread adoption of LIB-based electric vehicles. Subsequently, all-solid-state batteries (ASSBs) composed of solid electrolytes have emerged as a technology that can revolutionize the field of batteries. Inorganic solid electrolytes (such as oxides, sulfides, and halides) exhibit a low ignition risk, thereby ensuring safety, even under extreme conditions.[8−14] The advancement and implementation of ASSBs could address the low safety of LIB-based systems, facilitating progress and innovation in the electric-vehicle industry.

Sulfide-based solid-state electrolytes, particularly lithium thiophosphates, have been extensively used in ASSBs owing to their excellent ionic conductivity and composite-electrode-fabrication compatibility.[15−20] However, their electrochemical instability within the voltage range of LIBs causes decomposition during charge−discharge cycling. Additionally, the high chemical reactivity of sulfides causes undesirable electrolyte−electrode interfacial reactions, particularly at high voltages.[21−24] These interfacial reactions generate layers that adversely affect the movement of Li ions and electrons during battery cycling, leading to significant reductions in the storage capacity, rate capability, and cycling performance of ASSBs.

To mitigate these issues, several studies have attempted to reduce the reactivity of sulfide electrolytes. Consequently, sulfide electrolytes of the Li_6PS_5Cl (argyrodite) series, which exhibit a slightly lower ionic conductivity and higher interfacial cathode-compatibility than those of the $Li_{10}GeP_2S_{12}$ series (which exhibit an ionic conductivity comparable to that of liquid electrolytes), have been predominantly used in ASSBs.[18−20] Additionally, cathode coatings (with low sulfide-electrolyte reactivity and high ionic conductivity) that minimize the electrolyte−electrode interfacial reactions in the system have been used to construct practicable ASSBs. Notably, several widely used oxide coatings with low electronic conductivity alleviate the decomposition of sulfide electrolytes by limiting the electron exchange.[25−29] Although various ternary oxides[30−37] and polyanionic oxides[38,39] have been extensively investigated as cathode coatings, the effective

Received: November 29, 2023
Revised: January 3, 2024
Accepted: January 25, 2024
Published: February 5, 2024

https://doi.org/10.1021/acsomega.3c09545
ACS Omega 2024, 9, 8405−8416

control of interfacial reactions in ASSBs requires further investigation.

This study introduces a novel approach, precursor-based gradient doping using low-cost oxide-based materials followed by cathode fabrication, to synthesize cathodes that ensure minimal electrode−electrolyte reactions and facilitate interface stabilization. Cathodes fabricated by the newly proposed method showed minimal cathode−sulfide electrolyte interfacial reactions, enabling the construction of all-solid-state cells (ASSCs) with excellent electrochemical properties. Although lots of studies have investigated cathode doping in LIBs,[40−45] reports on cathode doping strategies for ASSBs (particularly for mitigating interfacial reactions with sulfide electrolytes) are relatively scarce. The critical requirement for protecting interfaces is the formation of thin and uniform coating layers, which has traditionally relied on expensive alkoxide-based source materials.[30,31,35,36] However, low-cost oxide-based materials have faced challenges in achieving sufficient coating effects due to the difficulty in forming a uniform coating layer. Here, as a new approach, oxide-based source materials for doping were mixed into the cathode precursor, which was subsequently mixed with the Li source and subjected to heat treatment. The goal of this method is to form a protective layer at the interface that can stabilize the cathode-sulfide electrolyte interface without utilizing alkoxide-based source materials. During heat treatment, Li (which exhibits facile diffusion) permeated the entire precursor material uniformly, whereas the heavy dopants (Nb, Ta, and La) showed gradient doping (generating precursors with a higher dopant concentration on the surface). These surface-oriented dopants protected the electrode interface by reducing electrode−electrolyte interfacial reactions. This newly proposed doping-based method for stabilizing the electrode−electrolyte interface in ASSB cathodes does not require any additional heat-treatment steps and utilizes low-cost source materials; therefore, it is more cost-effective than conventional coating methods used for ASSC electrodes and exhibits high potential for commercialization. A cost comparison of the alkoxide-based source materials typically used for electrode coatings and the oxide source materials used in this study are listed in Table S1. In this study, the newly proposed gradient-doping method was used to fabricate doped high-Ni cathodes (Ni content: >90%), which were used to construct cells containing sulfide solid electrolytes with the argyrodite structure. The electrochemical properties of the modified electrodes were analyzed using various experimental techniques. X-ray photoelectron spectroscopy (XPS) and transmission electron microscopy (TEM) analyses of composite electrodes comprising the doped cathodes and a sulfide electrolyte (extracted from ASSCs before and after charging and discharging) were used to confirm the efficacy of the newly proposed coating method and its advantages.

EXPERIMENTAL SECTION

The precursor ($Ni_{0.92}Co_{0.04}Mn_{0.04}(OH)_2$) was obtained from ECOPRO. To ensure a uniform distribution of the fine dopant within the precursor material, the dopants Nb_2O_5 (99.9%, Aldrich), Ta_2O_5 (99.5%, Aldrich), and La_2O_3 (99.9%, Aldrich) were ball milled at 500 rpm for 5 h and filtered through a 400-mesh sieve to extract particles with a size of $\lesssim$38 μm. To synthesize the undoped-cathode powder ($Li[Ni_{0.92}Co_{0.04}Mn_{0.04}]O_2$), a mixture comprising the precursor and LiOH in the molar ratio of 1:1.03 was heated at 500 °C for 5 h and calcined at 750 °C for 10 h under O_2 at a heating rate of 2 °C·min^{-1}. For gradient doping, the dopant powder (Nb_2O_5, Ta_2O_5, or La_2O_3) was added to the mixture comprising the precursor and LiOH, which was then heated and calcined (similar to the undoped-cathode synthesis). The dopant concentrations were adjusted to 0.5, 0.7, and 1.0 at. % of Nb; 0.1, 0.3, and 0.5 at. % of Ta; and 0.3, 0.5, and 0.7 at. % of La relative to the NCM cathode ($Li[Ni_{0.92}Co_{0.04}Mn_{0.04}]O_2$).

An X-ray diffractometer (Malvern Panalytical Empyrean) with monochromatized Cu Kα radiation (λ = 1.5406 Å) was used to record X-ray diffraction (XRD) data for the as-synthesized undoped- and doped-cathode powders over the 2θ range of 10−120°. The HighScore software was used to refine the lattice parameters for Rietveld refinement. The surface characteristics of the samples were investigated by scanning electron microscopy (SEM; JSM-7610F PLUS model). The presence of a coating layer on the doped cathodes was confirmed by scanning transmission electron microscopy (STEM) (JEM-2100F). XPS with a Thermo Scientific K-Alpha Plus system was used to investigate the dopant distribution on the surface of the doped-cathode powders. Ar-ion-gun etching of the samples enabled the acquisition of XPS spectra at varying depths, which were used to generate depth profiles of the dopants.

ASSCs comprising undoped and doped-NCM cathodes were constructed to investigate the influence of doping on the electrochemical performance of NCM cathodes. First, composite cathodes comprising an NCM powder (undoped or doped), a sulfide solid electrolyte (Li_6PS_5Cl, supplied by POSCO Jeong Kwan Co.), and carbon black (Super P) in the weight ratio of 60:36:4 were fabricated. To construct pressurized cells, the sulfide solid electrolyte (0.15 g) was first placed in a 13-pie mold and compressed (at 12 MPa), while the composite cathode material (0.015 g) was added to the opposite side of the mold and compressed at a high pressure of 44 MPa. Subsequently, after placing an Al foil (the current collector) and a Li-metal foil on opposite sides of the composite cathode, a 3-axis pressure of 50 kgf·cm^{-1} was applied on the assembled mold using a torque wrench. This process was conducted in a glovebox filled with high-purity Ar to prevent exposure to moisture and oxygen. Constant current densities in the voltage range of 2.52−4.32 V (vs Li) were used for discharge-capacity measurements at 30 °C, which were used to investigate the electrochemical performance of the as-constructed ASSCs (including their discharge behavior within the aforementioned voltage window).

An electrochemical workstation (AMETEK Versa STAT 3) was used to evaluate the impedance of the as-constructed ASSCs in the charged state after 1, 100, and 300 cycles; an AC voltage with an amplitude of 10 mV within the frequency range of 0.01 Hz to 500 kHz was used for experimentation. The impedance-fitting program ZsimpWin 3.60 was used for Nyquist-plot fitting. The galvanostatic intermittent titration technique (GITT) was used to analyze the Li^+-ion-diffusion characteristics after charge−discharge cycling with a pulse current of 0.1C intermittently for 10 min. GITT data were used to evaluate the contact area between the NCM material and sulfide solid electrolyte particles using the following equation

$$D_{Li^+} = \frac{4}{\pi\tau}\left(\frac{n_m V_m}{S}\right)^2\left(\frac{\Delta E_s}{\Delta E_t}\right)^2$$

https://doi.org/10.1021/acsomega.3c09545
ACS Omega 2024, 9, 8405−8416

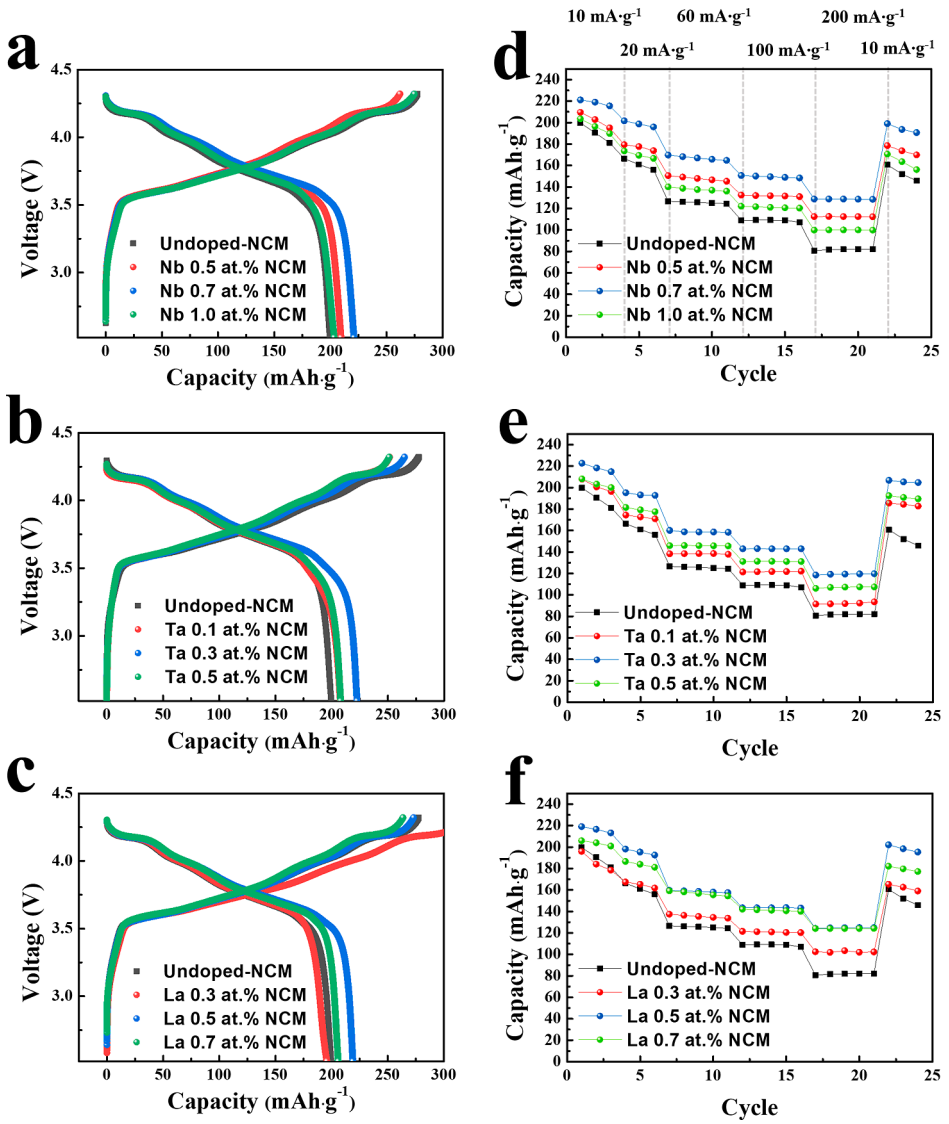

Figure 1. Initial charge−discharge profiles of (a) Nb-, (b) Ta-, and (c) La-doped NCM cathodes. Rate capabilities of (d) Nb-, (e) Ta-, and (f) La-doped NCM cathodes at current densities of 10, 20, 60, 100, and 200 mA·g^{-1}.

where D is the ion-diffusion coefficient of NCM, τ is the pulse duration (600 s), n_m is the molecular weight of the active material, V_m is the molar volume of the active material, S is the contact area between the solid electrolyte and the active material, ΔE_t is the transient voltage change, and ΔE_s is the steady-state voltage change.

XPS and TEM were used to investigate the cathode−electrolyte interface of the composite cathodes after 300 charge−discharge cycles. After Ar sputtering (to remove organic impurities from the sample surface using a GCIB of 8 keV for 60 s), the composite electrodes were vacuum transferred into the XPS system for analysis. A Quanta 3D FEG instrument was used to slice the composite electrode collected from ASSCs by using the focused ion beam (FIB) technique. A TitanTM 80-300 instrument was used to investigate the structural changes of the cathode after cycling. During FIB-based analysis, a vacuum-transfer TEM holder was used to maintain an inert atmosphere.

RESULTS AND DISCUSSION

Figure 1 shows a comparative analysis of the electrochemical performance of ASSCs containing cathodes doped with different amounts of Nb, Ta, and La. Figure 1a−c shows the initial charge−discharge profiles of the aforementioned ASSCs at a current density of 10 mA·g^{-1}. Notably, all the doped cathodes exhibit superior capacities to the undoped cathode, with distinct discharge-capacity variations that depend on the doping amount. Cathodes doped with 0.5, 0.7, and 1.0 at. % of Nb (Nb 0.5 at. % NCM, Nb 0.7 at. % NCM, and Nb 1.0 at. % NCM, respectively) show higher discharge capacities (209.5, 221.0, and 203.5 mA h·g^{-1}, respectively) than U-NCM (199.6 mA h·g^{-1}). The optimal Nb-doping concentration is 0.7 at. %; excess Nb doping (beyond 0.7 at. %) causes a rapid deterioration in the cathode capacity. Cathodes doped with 0.3 at. % of Ta (Ta 0.3 at. % NCM) and 0.5 at. % of La (La 0.5 at. % NCM) exhibit the highest discharge capacities (222.6 and 219.0 mA h·g^{-1}, respectively) among all the Ta- and La-doped cathodes, respectively, under the specified comparison conditions; excess Ta and La doping (beyond 0.3 and 0.5 at. %, respectively) causes a deterioration in the cathode capacity.

https://doi.org/10.1021/acsomega.3c09545
ACS Omega 2024, 9, 8405−8416

Table 1. Discharge Capacities (at Current Densities of 10, 20, 60, 100, and 200 mA·g^{-1}), Coulombic Efficiencies (at 10 mA·g^{-1}), and Capacity Retentions of Undoped and Doped NCM Cathodes

	discharge capacity (mA h·g^{-1})						
samples	10 mA·g^{-1} (1st cycle)	20 mA·g^{-1} (4th cycle)	60 mA·g^{-1} (7th cycle)	100 mA·g^{-1} (12th cycle)	200 mA·g^{-1} (17th cycle)	CE, η (%)	capacity retention (%)
U-NCM92	199.6	166.3	126.6	109.0	80.7	71.93	40.43
Nb 0.5 at.% NCM92	209.5	179.4	150.5	132.3	112.4	79.97	53.65
Nb 0.7 at.% NCM92	221.0	201.6	169.8	150.7	128.7	80.46	58.24
Nb 1.0 at.% NCM92	203.5	173.5	139.9	122.0	99.8	74.01	49.04
Ta 0.1 at.% NCM92	207.7	174.4	138.2	121.2	91.5	82.59	44.05
Ta 0.3 at.% NCM92	222.6	195.1	160.0	143.0	118.5	84.05	53.23
Ta 0.5 at.% NCM92	208.0	181.4	145.8	131.1	106.1	82.80	51.01
La 0.3 at.% NCM92	195.8	167.3	137.4	121.4	102.5	61.63	52.35
La 0.5 at.% NCM92	219.0	198.1	159.6	143.3	124.2	80.22	56.71
La 0.7 at.% NCM92	205.9	186.5	159.2	142.1	124.1	78.06	60.27

Figure 1d–f shows the rate capability analyses of the undoped and doped cathodes; the discharge capacities of the cathodes at current densities of 10, 20, 60, 100, and 200 mA·g^{-1} are summarized in Table 1. Remarkably, the discharge capacities of the doped cathodes consistently exceed that of the undoped cathode at all the current densities used for experimentation. Figure 1d shows that on increasing the current density, the discharge capacity of the undoped cathode reduces significantly (with values of 166.3, 126.6, 109.0, and 80.7 mA h·g^{-1} at 20, 60, 100, and 200 mA·g^{-1}, respectively), whereas that of the cathodes doped with 0.7 at. % of Nb notably enhances (with values of 201.6, 169.8, 150.7, and 128.7 mA h·g^{-1} at 20, 60, 100, and 200 mA·g^{-1}, respectively) under the same conditions. Therefore, the capacity retention (i.e., the percentage of capacity at 200 mA·g^{-1} relative to that at 10 mA·g^{-1}) of undoped cathodes (∼40.4%) is significantly lower than that of cathodes doped with 0.5, 0.7, and 1.0 at. % of Nb (∼53.7, ∼ 58.2, and ∼49.0%, respectively); this confirms that Nb doping improves the electrochemical properties of NCM cathodes. Additionally, the first-cycle Coulombic efficiency (CE) of the cathode improves significantly on Nb doping. The undoped cathode exhibits a CE of ∼72%, whereas cathodes doped with 0.5, 0.7, and 1.0 at. % of Nb show CE values of ∼80, ∼ 81%, and ∼74%, respectively.

Figure 1e.f indicates that Ta and La doping enhances the discharge capacity and rate capability of NCM cathodes. Cathodes doped with 0.3 at. % of Ta exhibit high discharge capacities of 195.1, 160.0, 143.0, and 118.5 mA h·g^{-1} at 20, 60, 100, and 200 mA·g^{-1}, respectively, along with significantly high values of capacity retention (∼53.2%) and CE (∼84.1%), outperforming the undoped cathode. Similarly, cathodes doped with 0.5 at. % of La exhibit high discharge capacities of 198.1, 159.6, 143.3, and 124.2 mA h·g^{-1} at 20, 60, 100, and 200 mA·g^{-1}, respectively, along with a capacity retention of 56.7% and CE of ∼80.2%, outperforming the undoped cathode. Therefore, Ta and La doping effectively improves the electrochemical properties of the NCM cathodes. The aforementioned results not only confirm the suitability of Nb-, Ta-, and La-doped cathode materials for ASSC applications but also highlight the critical significance of the doping level. In all cases, cathode doping beyond the optimal doping concentration caused a reduction in the cathode capacity, deteriorating the high rate performance of the cathode, possibly because surface layers comprising the excess doped ions impeded the smooth movement of Li ions and other charge carriers. Figure S1 shows a graph that compares the electrochemical performances of the undoped and optimally doped samples (Nb 0.7 at. % NCM, Ta 0.3 at. % NCM, and La 0.5 at. % NCM). Despite similar initial discharge rates, increasing the current density enhances the rate capability of Nb-doped cathodes to a slightly greater extent than those of the other optimally doped cathodes.

Comprehensive SEM and TEM analyses were used to understand the impact of diverse doping conditions on the surface morphology of the NCM-cathode powders. The SEM results shown in Figure S2 indicate that the surface characteristics of the cathode powder (comprising nano-granules) remain relatively stable on Nb doping. Although some heterogeneously shaped particles are observed on the surface of the powder, their origin (doping or residual impurities originating from the powder manufacturing process) is uncertain. Figure S3 indicates that the surface characteristics of cathode powders doped with 0.1 and 0.3 at. % of Ta are similar to those of the undoped sample (Figure S2a). However, cathode powders doped with 0.5 atom % of Ta contain nanoparticles affixed to the surface, potentially indicating that a portion of Ta_2O_5 did not sufficiently diffuse into the precursor. Differences in the surface characteristics of Nb- and Ta-doped cathode powders (despite the similar ionic radii of Nb^{5+} and Ta^{5+}) indicate that the diffusion of doping ions during heat treatment is influenced by several attributes of the dopant other than its ionic radius (such as the particle size and bond strength of oxides). Moreover, the aforementioned results indicate that Ta doping in large amounts is more challenging than that with Nb doping. Figure S4 shows that cathode powders doped with 0.7 at. % of La contain surface nanoparticles as well. Moreover, even at low levels of doping (0.3 and 0.5 at. %), La-doped cathodes exhibit a slightly higher roughness than the undoped cathode. This can be attributed to limited La^{3+} diffusion owing to the large ionic radius of La^{3+} (116 pm), which is significantly larger than the ionic radii of Nb^{5+} and Ta^{5+}.

Along with surface irregularities, cathode powders doped with 0.5 at. % of Ta and 0.7 at. % of La show lower discharge capacities and rate capabilities than those doped with 0.3 at. % of Ta and 0.5 at. % of La. However, despite a smooth surface, cathode powders doped with 1.0 atom % of Nb show a poorer electrochemical performance than those doped with 0.7 atom % of Nb, possibly because excess doping causes an accumulation of the oxide-dopant source on the cathode surface, hindering the movement of Li and electrons. Notably, insufficient doping also hinders the movement of ions and

https://doi.org/10.1021/acsomega.3c09545
ACS Omega 2024, 9, 8405−8416

electrons. Under the experimental conditions used in this study, 0.7 at. % of Nb, 0.3 at. % of Ta, and 0.5 at. % of La were identified as the optimal doping amounts. Hereafter, Nb-NCM, Ta-NCM, and La-NCM refer to the three optimally doped samples (cathodes doped with 0.7 at. % of Nb, 0.3 at. % of Ta, and 0.5 at. % of La, respectively), while U-NCM indicates the uncoated sample. Figure 2 shows the results of

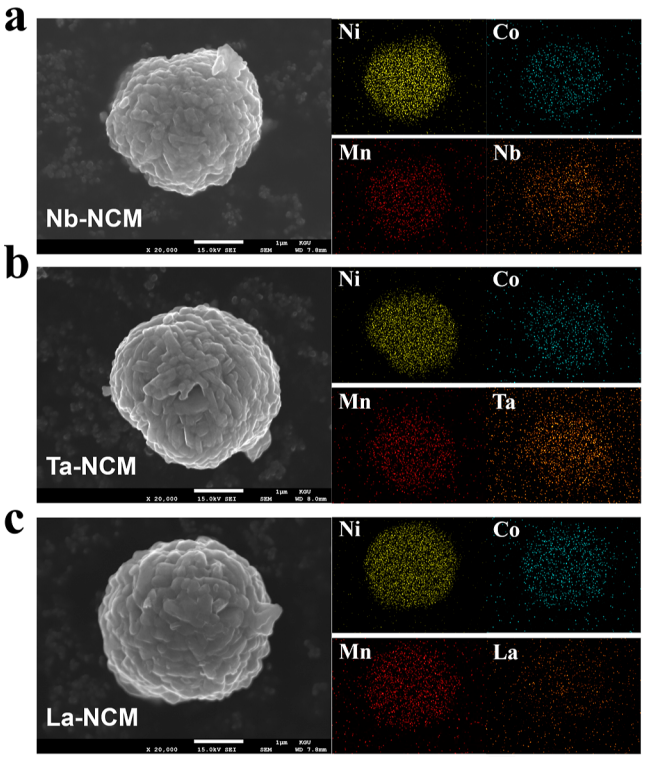

Figure 2. SEM images (left) and EDS mappings (right) of NCM cathodes doped with (a) 0.7 at. % of Nb, (b) 0.3 at. % of Ta, and (c) 0.5 at. % of La.

the SEM−EDS analyses of Nb-, Ta-, and La-NCM; EDS element mapping indicates the presence of Ni, Co, and Mn and the doping element (Nb, Ta, and La, respectively) in the samples.

TEM was used to investigate the surface alterations caused by doping (Figure 3a−d). Prior to analysis, all samples were washed for 5 min to remove any potential Li-based impurity layers (such as Li_2CO_3 and LiOH) that could hinder the observation of the coating layer. No discernible heterogeneous layers were observed on U-NCM, whereas a thin layer (~2−3 nm in thickness, possibly formed during the doping process) was observed on the doped samples. The surface layers of Nb- and Ta-NCM were uniform, whereas that of La-NCM was rough, consistent with the SEM images of these samples (Figure S4b). TEM indicated that a portion of the dopant material possibly concentrated on the cathode surface, forming a coating-like layer, which minimized electrode−electrolyte interfacial reactions by controlling side reactions of the cathode with the sulfide electrolyte, similar to traditional surface coatings. Therefore, the improvements in the electrochemical properties of NCM cathodes on doping (shown in Figure 1) could be attributed to alterations in the bulk characteristics (similar to the effects of conventional doping) and the presence of a surface layer that functioned as a protective coating.

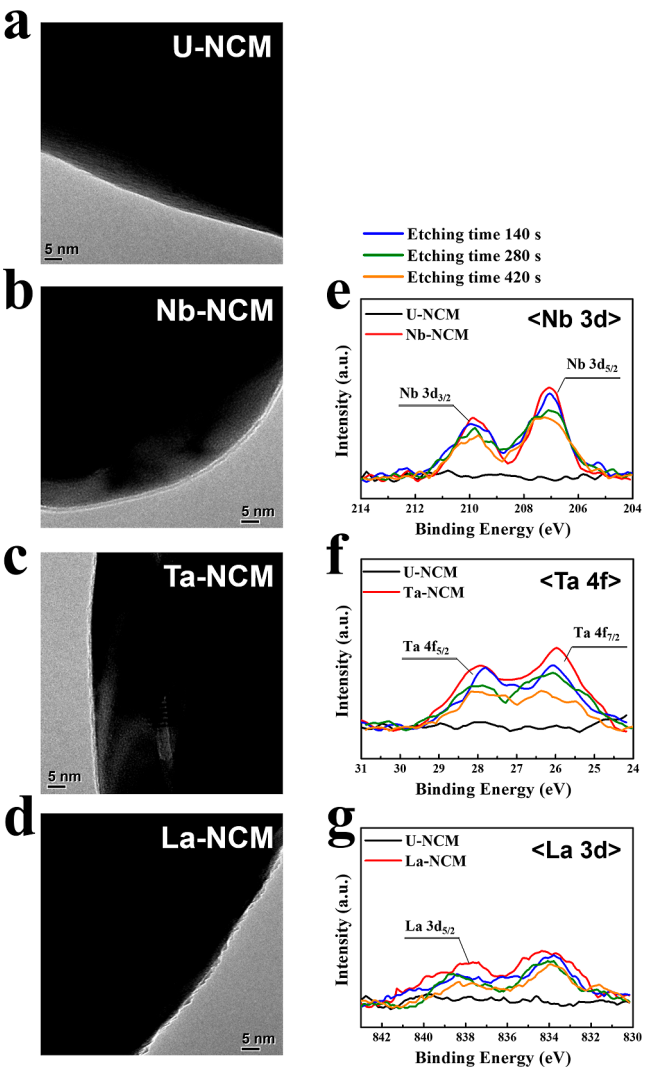

Figure 3. TEM images of (a) U-NCM, (b) Nb-NCM, (c) Ta-NCM, and (d) La-NCM. XPS spectra of (e) Nb-NCM, (f) Ta-NCM, and (g) La-NCM after etching.

The pronounced concentration at the surface raises the hypothesis that the dopant is arranged in a gradient configuration. To validate this, surface XPS analysis of the coated samples was conducted. Figure 3e−g shows the XPS profiles of Nb-NCM, Ta-NCM, and La-NCM after ion-gun etching for 40, 140, 280, and 420 s, which were used to estimate the dopant concentrations at different depths in the doped cathodes. Figure 3e shows that the XPS spectrum of U-NCM contains no discernible peaks, whereas that of Nb-NCM contains distinct peaks corresponding to Nb $3d_{3/2}$ and $3d_{5/2}$. Notably, the peak intensities decrease on increasing the etching time, indicating a decrease in the Nb concentration with depth. Figure 3f indicates a decrease in the peak intensities corresponding to Ta $4f_{5/2}$ and $4f_{7/2}$ on prolonged etching. As shown in Figure 3g, despite the lower intensities of the $3d_{5/2}$ peaks of La compared to those of Nb and Ta, their intensities decrease on etching. The aforementioned results indicate a higher dopant concentration on the doped-cathode surface than in the interior, confirming the formation of a surface-coating layer (or at least a dopant concentration gradient). The composition of the surface layer (which functioned as a protective barrier, minimizing undesirable reactions between

https://doi.org/10.1021/acsomega.3c09545
ACS Omega 2024, 9, 8405−8416

the cathode and sulfide electrolyte) could not be accurately determined in this study; it possibly comprised various oxides (such as Li−Nb−O, Li−Ta−O, and La−La−O) formed by interactions of the surface dopant with Li and O.

XRD with Rietveld refinement was used to investigate the effects of doping on the crystal structure of the NCM cathodes. Figure 4a indicates that the XRD patterns of the doped and undoped cathodes are similar (with slightly different peak intensities and positions). Table 2 summarizes the crystal-structure parameters and $I_{(003)}/I_{(104)}$ values of the doped and undoped cathodes estimated by the Rietveld refinement of their XRD data (Figure S5). Although the lattice parameters of the doped samples differ from those of the undoped sample owing to the influence of dopants, the differences are not statistically significant. The $I_{(003)}/I_{(104)}$ ratios of Nb-NCM and Ta-NCM are slightly higher than that of U-NCM, indicating a reduction in cation-mixing with Nb and Ta doping. Cation mixing, which involves the substitution of Li sites within the cathode material by Ni ions, adversely affects the rate capability of the cathode by hindering the diffusion of Li during charge−discharge. The reduction in cation mixing on Nb and Ta doping indicates that these dopants enhance the rate capability of NCM cathodes (in terms of bulk characteristics), improving their rate capability, as indicated by the discharge-capacity measurements at various current densities shown in Figure 1d,e. Interestingly, despite a lower $I_{(003)}/I_{(104)}$ ratio, La-NCM showed a higher rate capability than U-NCM (Figure 1f), possibly because the stabilization of side reactions at the cathode−electrolyte interface influenced the rate capability more significantly than the bulk properties of the material. Therefore, despite no reduction in cation mixing, La doping caused interface stabilization by the formation of a protective surface layer.

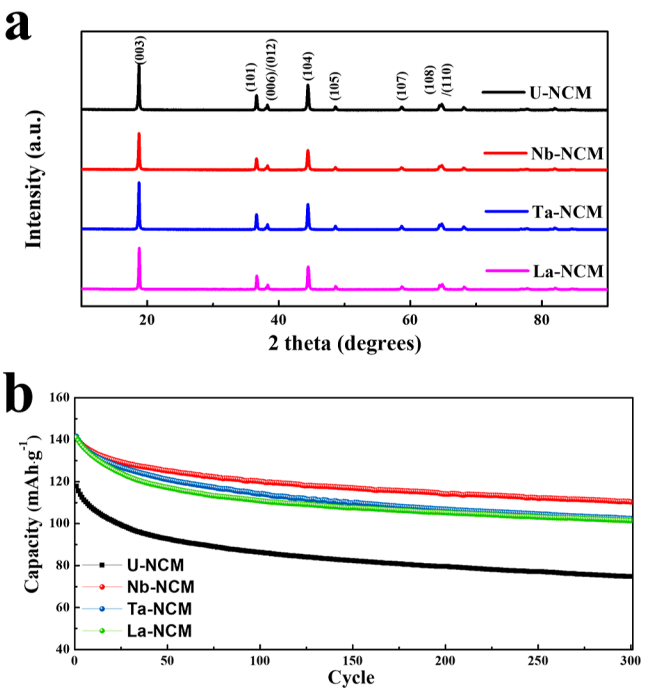

Figure 4. (a) XRD patterns and (b) cyclic performances of undoped and doped NCM cathodes at a current density of 400 mA·g^{-1} (~2C rate).

Figure 4b shows a comparison of the cyclic performances of U-NCM, Nb-NCM, Ta-NCM, and La-NCM at a current density of 400 mA·g^{-1} over 300 cycles. With cycling, the discharge capacities of all of the samples gradually decrease. After 300 cycles, U-NCM retains ~63% of its initial discharge capacity, while Ta-NCM, La-NCM, and Nb-NCM exhibit relatively higher capacity retentions of ~73, 72, and 78%, respectively. The capacity loss in ASSBs during cycling can be attributed to several factors. First, the formation of a cathode−electrolyte interfacial-reaction layer owing to side reactions between the cathode material and electrolyte during cycling adversely affects the electrochemical performance of ASSBs.[25,26,28] Additionally, the expansion and contraction of the cathode material during charge−discharge cycling causes a loss of contact between the cathode and solid electrolyte owing to the detachment of the former from the latter, decreasing the discharge capacity of the system, thereby reducing the overall battery performance.[23,26,28] In this study, cathode-material degradation during cycling was mitigated by the introduction of dopants (Nb, Ta, and La) into the cathode. Moreover, the formation of an interfacial protective layer (which functioned as a barrier, minimizing side reactions and maintaining good contact between the cathode and solid electrolyte) through gradient doping significantly enhanced the stability of the cathode−electrolyte interface. Therefore, despite the occurrence of contact-related issues, reduced cathode degradation and improved interfacial stability enabled the doped cathodes to exhibit excellent cyclic performance. Improved stability of the cathode structure by dopants is also likely to affect the cyclic performance. It has been reported that the doping of Ta^{5+} and Nb^{5+} reduces O_2 emission at a high voltage and reduces the proportion of Ni^{3+} due to high oxidation number, which contributes to the stability of the NCM cathode.[40−43] In the case of La^{3+} doping, although the oxidation number is not high, it has been reported that it can contribute to the improvement of the stability of the host structure and reduce the microcracks generated during the charge−discharge process.[44,45] This improvement in bulk properties may have lowered the degradation of the cathode during the charge and discharge process and positively affected the cycle life. The advantage of the gradient doping used in this study is that the interfacial protective layer effect and bulk property improvement by doping can be obtained simultaneously.

The Nyquist plots shown in Figure 5a−d offer insights into the interfacial-resistance changes of NCM cathodes with

Table 2. Crystal-Structure Parameters and $I_{(003)}/I_{(104)}$ Values of U-NCM, Nb-NCM, Ta-NCM, and La-NCM Estimated by Rietveld Refinement

sample	R_{wp} (%)	GOF	a (Å)	c (Å)	V (Å)	c/a	$I_{(003)}/I_{(104)}$
U-NCM	4.6873	1.299	2.8747	14.1949	101.5893	4.9379	1.4914
Nb-NCM	4.6839	1.224	2.8754	14.1985	101.6646	4.9379	1.5583
Ta-NCM	4.6006	1.261	2.8749	14.1963	101.6135	4.9380	1.5537
La-NCM	5.3359	1.364	2.8739	14.1943	101.5285	4.9390	1.4720

https://doi.org/10.1021/acsomega.3c09545
ACS Omega 2024, 9, 8405−8416

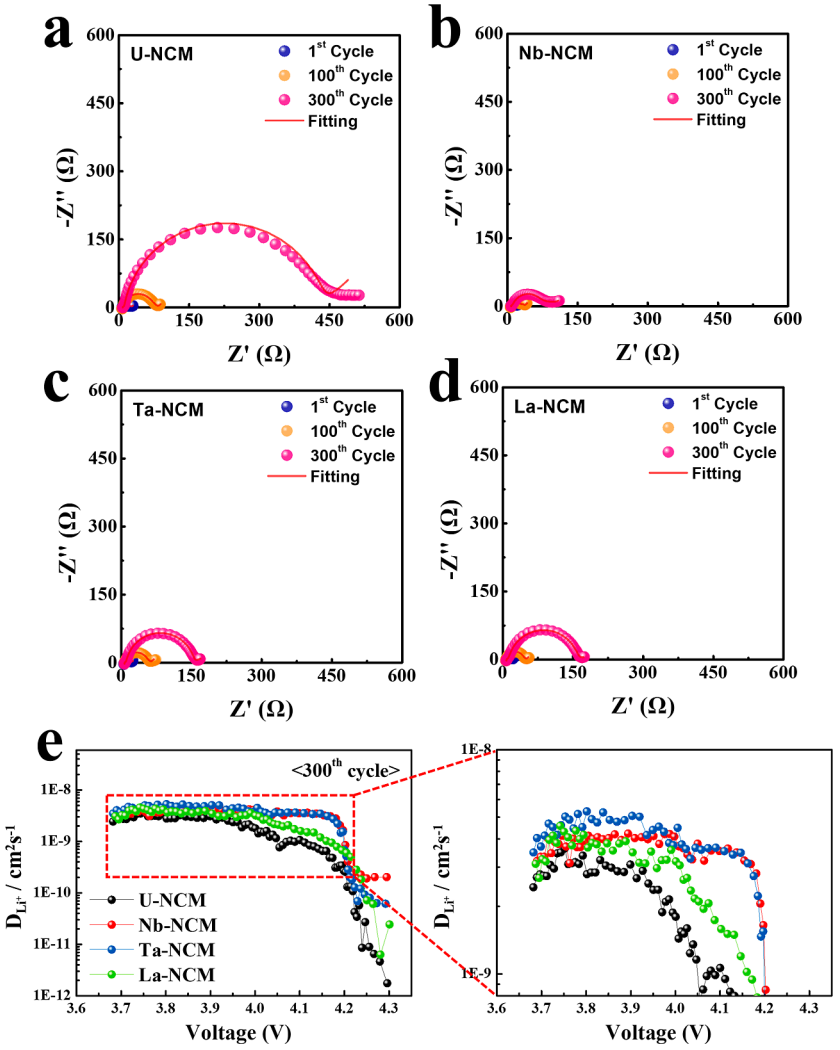

Figure 5. Nyquist plots of (a) U-NCM, (b) Nb-NCM, (c) Ta-NCM, and (d) La-NCM after 1, 100, and 300 cycles. (e) Li-diffusion coefficients (D_{Li+}) estimated from GITT curves measured after 300 cycles.

Table 3. Impedance Values Were Calculated from the Nyquist Plots for U-NCM, Nb-NCM, Ta-NCM, and La-NCM

	After 1st cycle			After 100th cycle			After 300th cycle			
samples	$R_{SE,bulk}$ (Ω)	$R_{SE,gb}$ (Ω)	$R_{electrode/SE}$ (Ω)	$R_{SE,bulk}$ (Ω)	$R_{SE,gb}$ (Ω)	$R_{electrode/SE}$ (Ω)	$R_{SE,bulk}$ (Ω)	$R_{SE,gb}$ (Ω)	$R_{electrode/SE}$ (Ω)	R_{total} (Ω)
U-NCM	7.4	3.8	17.3	8.3	2.8	74.6	8.4	4.2	447.7	460.3
Nb-NCM	7.7	3.6	11.9	8.4	4.1	26.8	8.4	5.5	87.4	101.3
Ta-NCM	7.6	4.0	12.0	7.7	3.0	55.9	7.6	4.7	151.9	164.2
La-NCM	7.6	4.0	11.2	7.4	3.1	41.8	8.1	5.9	155.6	169.6

gradient doping. Figure 5a shows that the semicircle size corresponding to cells containing U-NCM expands significantly after 100 and 300 charge−discharge cycles. This indicates a large increase in the impedance and degradation of the cathode−electrolyte interface during cycling owing to the formation of an interfacial-reaction layer that hinders ion and electron transport. Cells containing gradient-doped samples (Nb-NCM, Ta-NCM, and La-NCM) show smaller semicircle-size increments in comparison to those containing U-NCM during cycling (Figures 5b−d and S6). Therefore, the gradient-doping strategy proposed in this study mitigates the increase in the impedance of NCM cathodes during cycling. Gradient dopants maintain a stable and conducive cathode−electrolyte interface, resulting in good interfacial properties and a low impedance growth. Nyquist-plot fitting was used to estimate the impedance values of ASSCs comprising doped and undoped cathodes. The equivalent circuit used in the fitting and a Bode plot with the fitting results are displayed in Figure S7. Table 3 summarizes the impedance values of these cells, which are categorized as bulk resistance ($R_{SE,bulk}$), the grain-boundary resistance of the sulfide electrolyte ($R_{SE,gb}$), resistance at the cathode−electrolyte ($R_{cathode/SE}$) and anode−electrolyte ($R_{anode/SE}$) interfaces, and the Warburg impedance (W).[23,29,32,46−51] As it is difficult to separate $R_{cathode/SE}$ and $R_{anode/SE}$ in practice, their combination is represented by $R_{electrode/SE}$, which indicates the cathode−electrolyte's interfacial stability. Cells containing U-NCM exhibit significantly higher $R_{electrode/SE}$ values (~17.3, ~74.6, and ~447.7 after 1, 100, and 300 cycles, respectively) than those containing gradient-doped NCMs; cells containing Nb-NCM show

https://doi.org/10.1021/acsomega.3c09545
ACS Omega 2024, 9, 8405−8416

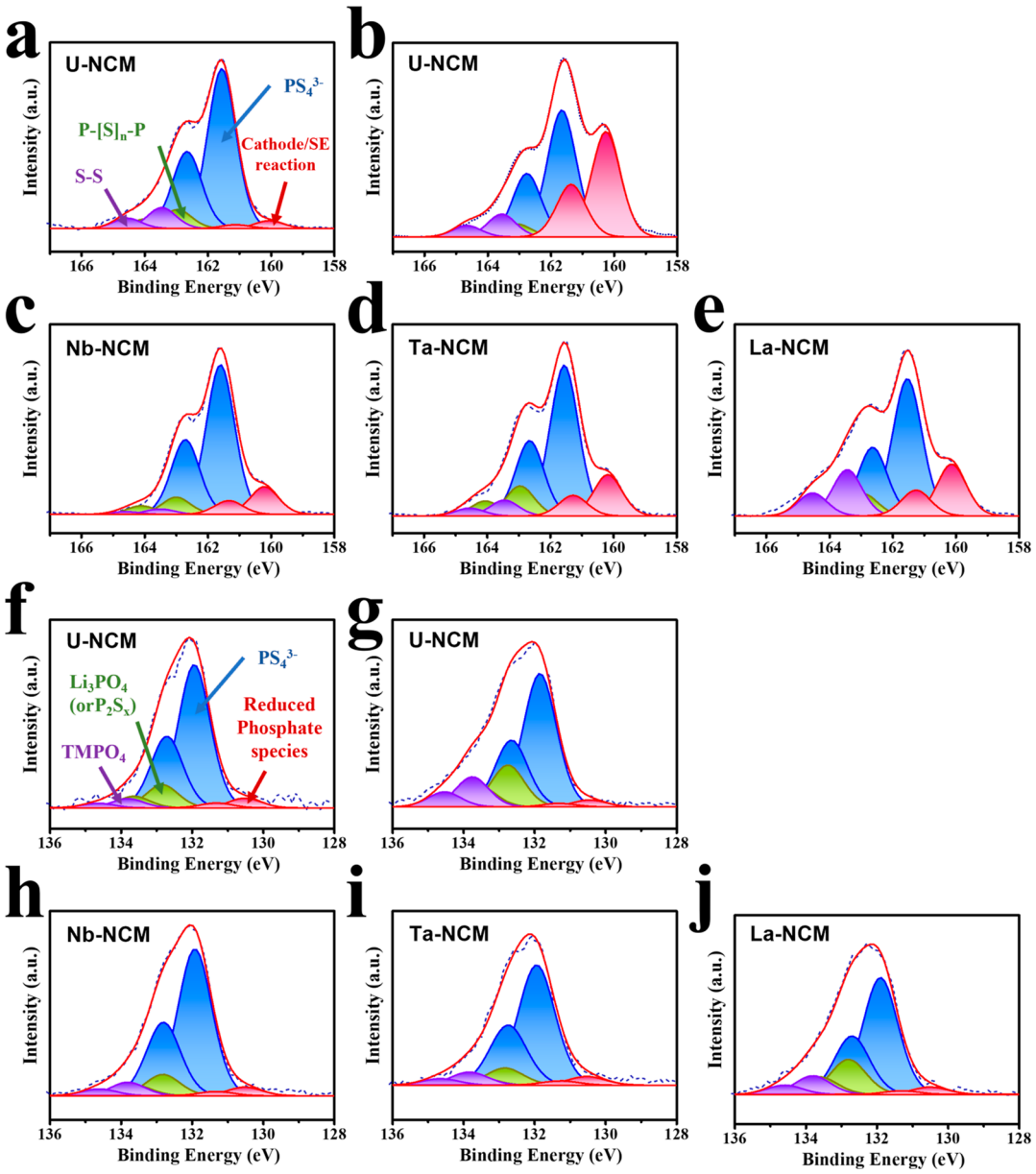

Figure 6. XPS profiles of NCM cathodes. (a) S 2p spectrum of U-NCM before cycling. S 2p spectrum of (b) U-NCM, (c) Nb-NCM, (d) Ta-NCM, and (e) La-NCM after 300 charge−discharge cycles. (f) P 2p spectrum of U-NCM before cycling. P 2p spectrum of (g) U-NCM, (h) Nb-NCM, (i) Ta-NCM, and (j) La-NCM after 300 charge−discharge cycles.

significantly low $R_{electrode/SE}$ values (~11.9, ~26.8, and ~87.4 after 1, 100, and 300 cycles, respectively). The significant reduction in $R_{electrode/SE}$ on gradient doping indicates the stabilization of the cathode−sulfide electrolyte interface on doping. $R_{anode/SE}$ is assumed to be negligibly influenced by doping; therefore, the substantial decrease in $R_{electrode/SE}$ on doping can be mainly attributed to interfacial stabilization at the cathodes owing to gradient doping. Ta-, La-NCMS also showed a reduction in $R_{electrode/SE}$, but not as much as Nb doping.

Figure 5e shows GITT curves measured after 300 charge−discharge cycles, which were used to estimate the Li-diffusion coefficient (D_{Li+}) values of doped and undoped cathodes in the voltage range of 3.7−4.3 V (to investigate the influence of gradient doping on Li^+ diffusion). Figure S8 indicates that gradient-doped NCMs (particularly Nb-NCM and Ta-NCM) exhibit D_{Li+} values higher than those of U-NCM over the entire experimental voltage range. At ~3.7 and 4.1 V, the D_{Li+} values of U-NCM are 2.7×10^{-9} and 9.5×10^{-10} $cm^2 \cdot s^{-1}$, respectively, those of Ta-NCM are 4.1×10^{-9} and 3.5×10^{-9} $cm^2 \cdot s^{-1}$, respectively, and those of Nb-NCM are 4.00×10^{-9} and 3.6×10^{-9} $cm^2 \cdot s^{-1}$, respectively. Thus, doping increases the efficiency of Li^+ diffusion, possibly due to interfacial stabilization and a change in bulk properties due to doping.

XPS, which can identify the reaction products generated by charging and discharging, is commonly used to investigate interfacial side reactions. In this study, to confirm the side-reaction products generated during cycling, XPS was used to analyze composite electrodes after 300 charge−discharge cycles. Figure 6a shows the S 2p XPS spectrum of the U-NCM before cycling. The principal peaks at binding energies of 161.6 and 162.7 eV (corresponding to the S $2p_{3/2}$ and S $2p_{1/2}$ constituents, respectively) can be attributed to PS_4^{3-} bonds, which are intrinsic to the sulfide−electrolyte matrix.[46,52]

https://doi.org/10.1021/acsomega.3c09545
ACS Omega 2024, 9, 8405−8416

The red peaks at 160.2 and 161.3 eV can be attributed to lithium sulfide (Li_2S)[53−55] or transition-metal sulfides that are generated by the chemical mixing of transition-metal ions (within the cathode) and sulfide components (within the electrolyte).[25,26] The green doublets (at 163.0 and 164.1 eV) and violet peaks (at 163.5 and 164.6 eV) correspond to P−[S]n−P and S−S bonds, respectively,[36,52] formed by sulfide−electrolyte oxidation. Figure 6b indicates that the S 2p XPS spectrum of U-NCM undergoes significant changes after 300 charge−discharge cycles. The intensity of the principal peaks (corresponding to PS_4^{3-} bonds within the sulfide electrolyte) and red peaks (corresponding to chemical reactions between the cathode and electrolyte) significantly decreases and increases, respectively. These changes indicate that active chemical mixing (between S^{2-} and P^{x-} ions in the electrolyte and between O^{2-} ions and transition-metal ions from the cathode) results in the formation of side-reaction products (such as Li_2S, NiS, Ni_3S_4, Mn_2S_3, MnS, and CoS).[21−23] Figure 6c−e, which shows the S 2p XPS profiles of the gradient-doped samples after cycles, indicates a significant reduction in the intensity of the red peaks. Among the dopants, Nb and La caused the maximum and minimum peak-intensity reductions, respectively (Figure S9). Thus, gradient doping effectively minimized cathode−electrolyte side reactions, producing significantly low amounts of sulfide products.

Figure 6f shows the P 2p spectrum of U-NCM before cycling. The main peaks corresponding to PS_4^{3-} bonds appear at 131.9 and 132.7 eV.[30,56] Red peaks at 130.5 and 131.3 eV indicate the formation of reduced phosphate species owing to the decomposition of the sulfide electrolyte.[57] Violet peaks at 133.8 and 134.6 eV indicate the formation of transition-metal phosphates owing to chemical mixing at the cathode−sulfide electrolyte interface, while green peaks at 132.8 and 133.6 eV indicate the formation of Li_3PO_4 or P_2S_x due to side reactions. Figure 6g shows that the intensity of the violet and green peaks increases significantly after 300 charge−discharge cycles, confirming continuous chemical mixing and side reactions between the cathode and sulfide electrolyte. Notably, the violet and green peaks in the P 2p spectra of the gradient-doped samples exhibit a significantly lower intensity than those in the spectrum of the undoped sample (Figures 6h−j and S10), confirming that doping (particularly Nb doping) effectively suppresses cathode−electrolyte side reactions. The suppression of side reactions is crucial for improving the overall performance and longevity of ASSBs.

The TEM analysis of postcycling composite electrodes was used to investigate the potential of gradient doping to mitigate electrode−electrolyte side reactions and cathode degradation. The ability of gradient doping to suppress chemical mixing (including the diffusion of oxygen from the cathode toward the solid electrolyte), which contributes significantly to cathode degradation, was investigated by comparing the properties of U-NCM with those of Nb-NCM (which exhibited the best doping effect). Figure 7a shows the TEM images and spot-pattern analyses of a composite electrode comprising U-NCM, before and after 300 charge−discharge cycles. Initially, a distinct boundary is observed between the cathode and solid electrolyte, which blurs on cycling. Additionally, the interior of the powder exhibits the characteristic spot pattern of a layered structure, whereas the surface shows a different spot pattern, indicating surface-layer degradation on cycling, which can be primarily (or at least partially) attributed to chemical mixing. The surface-degradation layer shows a thickness of ∼12−13 nm. Figure 7b indicates that Nb-NCM also exhibits a surface-degradation layer (with a thickness of ∼5−6 nm). The significantly lower thickness of the surface-degradation layer in Nb-NCM compared to that in U-NCM can be attributed to the reduced diffusion of oxygen ions from the cathode toward the solid electrolyte in the former. Therefore, gradient doping effectively suppresses cathode−electrolyte side reactions, improving the electrochemical properties of doped samples compared to those of U-NCM. The effect of gradient doping on ASSCs with NCM cathodes is summarized schematically in Figure 8.

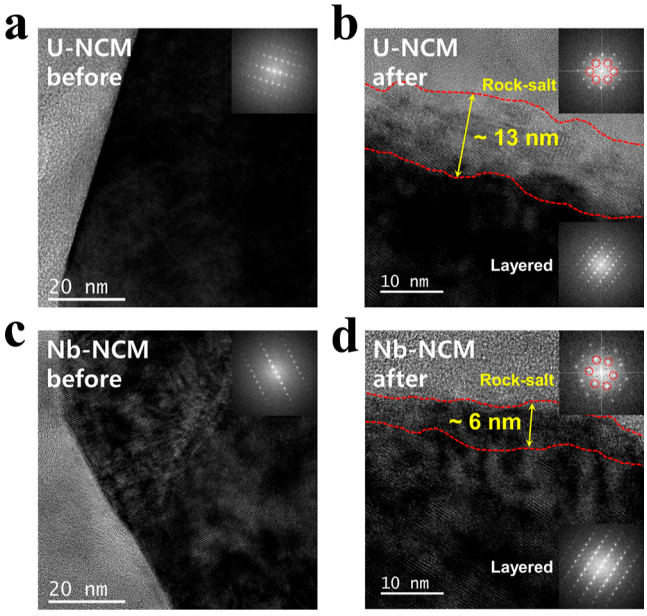

Figure 7. Cross-sectional high-resolution TEM images of the cathode−sulfide electrolyte interface for U-NCM [(a) before and (b) after 300 charge−discharge cycles] and Nb-NCM [(c) before and (d) after 300 charge−discharge cycles].

CONCLUSIONS

In summary, gradient doping with Nb, Ta, or La was used to fabricate high-Ni NCM cathodes with a high cathode−sulfide electrolyte interfacial stability. Unlike conventional surface-coating strategies, which depend on high-cost source materials to generate uniform and thin coating layers, precursor-stage doping with cost-effective oxide materials Nb_2O_5, Ta_2O_5, and La_2O_3 was used for cathode coating in this study. The discharge capacity and rate capability of ASSCs comprising doped cathodes were higher than those comprising undoped cathodes; cells comprising optimally doped cathodes (cathodes doped with 0.7 at. % of Nb, 0.3 at. % of Ta, and 0.5 at. % of La) showed the best electrochemical properties. SEM, TEM, and XPS analyses were used to investigate the surface enrichment of Nb, Ta, and La in the doped cathodes; relatively low concentrations of the dopant were observed in the interior of the cathodes, confirming a gradient dopant distribution. According to XRD and GITT analyses, Nb and Ta doping significantly reduced cation mixing. Notably, all three types of doped cathodes (Nb-, Ta-, and La-NCM) showed a higher ion diffusivity and cycling stability and lower impedance resistance than U-NCM. XPS confirmed the lesser production of side-reaction products by interfacial reactions in the doped cathodes than in U-NCM after cycling. Additionally,

https://doi.org/10.1021/acsomega.3c09545
ACS Omega 2024, 9, 8405−8416

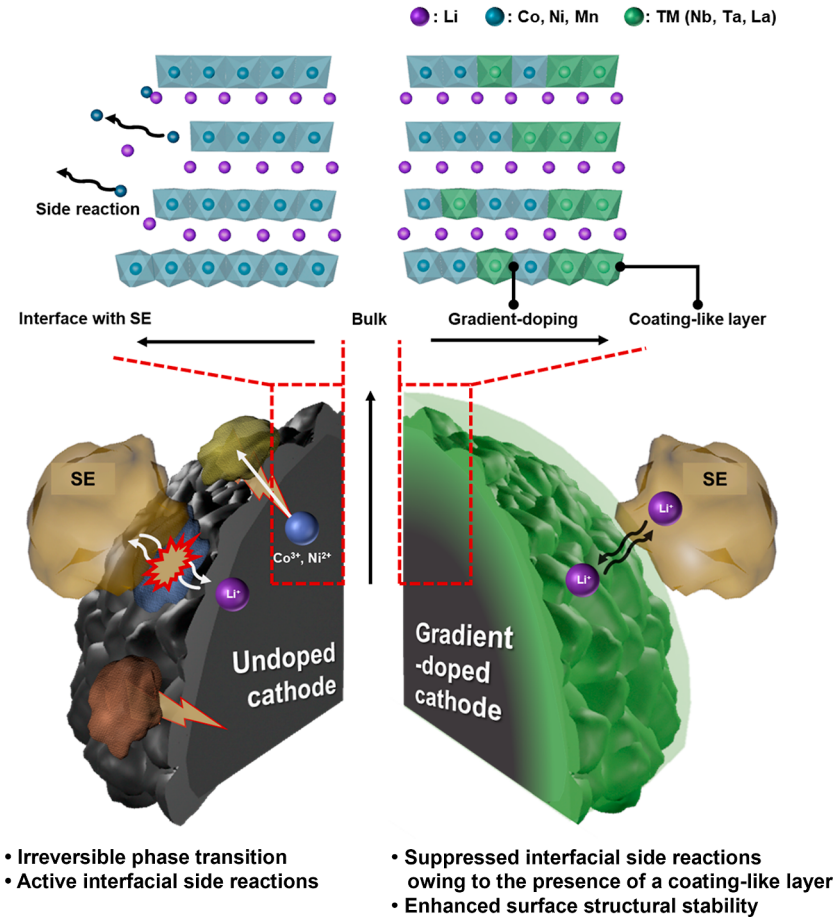

Figure 8. Schematic illustration of the effects of gradient doping on ASSB cathodes.

TEM confirmed lower cathode-interface degradation in the doped cathodes than in U-NCM after charge−discharge cycling. This phenomenon can be attributed to the enhanced structural stability of the cathode−electrolyte interface owing to doping and the formation of an interfacial layer owing to gradient doping. This study contributes significantly to ASSB research, and the cost-effective and efficient strategy for controlling interfacial reactions and enhancing the performance of ASSCs proposed in this study could facilitate the development of stable and high-performance ASSB technologies in the future.

■ ASSOCIATED CONTENT

Supporting Information

The Supporting Information is available free of charge at https://pubs.acs.org/doi/10.1021/acsomega.3c09545.

Additional experimental details, including electrochemical performance, SEM images, Rietveld refinement results, Nyquist plots, comparison of the D_{Li+} values, and XPS spectra of doped and undoped cathodes fabricated in this study (PDF)

■ AUTHOR INFORMATION

Corresponding Author

Yong Joon Park − *Department of Advanced Materials Engineering, Kyonggi University, Suwon-Si, Gyeonggi-Do 16227, Republic of Korea;* orcid.org/0000-0003-4388-3440; Phone: +82-31-249-9769; Email: yjpark2006@kyonggi.ac.kr

Author

Yong Jun Ji − *Department of Advanced Materials Engineering, Kyonggi University, Suwon-Si, Gyeonggi-Do 16227, Republic of Korea*

Complete contact information is available at: https://pubs.acs.org/10.1021/acsomega.3c09545

Author Contributions

Yong Jun Ji: Conceptualization; Investigation; Data curation, Writing—Original draft preparation. **Yong Joon Park**: Conceptualization; Writing—Reviewing and Editing; Supervision; Funding acquisition; project administration. The manuscript was written with contributions from all authors. All authors approved the final version of the manuscript.

Notes

The authors declare no competing financial interest.

■ ACKNOWLEDGMENTS

This study was supported by the Materials and Components Technology Development Program of MOTIE/KEIT (grant no. 20009957) and a National Research Foundation of Korea (NRF) grant funded by the Korean government (MSIT, no. 2023R1A2C1003330). This work was also supported by the Materials and Components Technology Development Program (grant no. 20024249) funded By the Ministry of Trade, Industry & Energy (MOTIE, Korea) and Korea Institute for

https://doi.org/10.1021/acsomega.3c09545
ACS Omega 2024, 9, 8405−8416

Advancement of Technology (KIAT) grant funded by the Korean Government (MOTIE) (P0020614, HRD Program for Industrial Innovation).

■ ABBREVIATIONS

XPS, X-ray photoelectron spectroscopy; EDS, energy-dispersive X-ray spectroscopy; SEM, scanning electron microscopy; TEM, transmission electron microscopy; ASSB, all-solid-state battery; ASSC, all-solid-state cell; LIB, lithium-ion battery

■ REFERENCES

(1) Brow, R.; Donakowski, A.; Mesnier, A.; Pereira, D. J.; Steirer, K. X.; Santhanagopalan, S.; Manthiram, A. Mechanical Pulverization of Co-Free Nickel-Rich Cathodes for Improved High-Voltage Cycling of Lithium-Ion Batteries. *ACS Appl. Energy Mater.* **2022**, *5* (6), 6996−7005.

(2) Liu, S.; Kang, L.; Hu, J.; Jung, E.; Henzie, J.; Alowasheeir, A.; Zhang, J.; Miao, L.; Yamauchi, Y.; Jun, S. C. Realizing Superior Redox Kinetics of Hollow Bimetallic Sulfide Nanoarchitectures by Defect-Induced Manipulation toward Flexible Solid-State Supercapacitors. *Small* **2022**, *18* (5), 2104507.

(3) Liu, S.; Kang, L.; Henzie, J.; Zhang, J.; Ha, J.; Amin, M. A.; Hossain, M. S. A.; Jun, S. C.; Yamauchi, Y. Recent Advances and Perspectives of Battery-Type Anode Materials for Potassium Ion Storage. *ACS Nano* **2021**, *15* (12), 18931−18973.

(4) Li, Q.; Deng, R.; Chen, Y.; Gong, J.; Wang, P.; Zheng, Q.; Huo, Y.; Xie, F.; Wei, X.; Yang, C.; Lin, D. Homologous Heterostructured NiS/NiS_2@C Hollow Ultrathin Microspheres with Interfacial Electron Redistribution for High-Performance Sodium Storage. *Small* **2023**, *19*, 2303642.

(5) Liu, S.; Kang, L.; Jun, S. C. Challenges and Strategies toward Cathode Materials for Rechargeable Potassium-Ion Batteries. *Adv. Mater.* **2021**, *33* (47), 2004689.

(6) Kaneda, H.; Furuichi, Y.; Ikezawa, A.; Arai, H. Single-Crystal-like Durable $LiNiO_2$ Positive Electrode Materials for Lithium-Ion Batteries. *ACS Appl. Mater. Interfaces* **2022**, *14* (47), 52766−52778.

(7) Im, H. J.; Park, Y. J. Interfacial Stabilization of Li_2O-Based Cathodes by Malonic-Acid-Functionalized Fullerenes as a Superoxo-Radical Scavenger for Suppressing Parasitic Reactions. *ACS Appl. Mater. Interfaces* **2022**, *14* (34), 38952−38962.

(8) Pervez, S. A.; Cambaz, M. A.; Thangadurai, V.; Fichtner, M. Interface in Solid-State Lithium Battery: Challenges, Progress, and Outlook. *ACS Appl. Mater. Interfaces* **2019**, *11*, 22029−22050.

(9) Zheng, Y.; Yao, Y.; Ou, J.; Li, M.; Luo, D.; Dou, H.; Li, Z.; Amine, K.; Yu, A.; Chen, Z. A Review of Composite Solid-State Electrolytes for Lithium Batteries: Fundamentals, Key Materials and Advanced Structures. *Chem. Soc. Rev.* **2020**, *49* (23), 8790−8839.

(10) Ma, M.; Zhang, M.; Jiang, B.; Du, Y.; Hu, B.; Sun, C. A Review of All-Solid-State Electrolytes for Lithium Batteries: High-Voltage Cathode Materials, Solid-State Electrolytes and Electrode-Electrolyte Interfaces. *Mater. Chem. Front.* **2023**, *7* (7), 1268−1297.

(11) Sun, Y. K. Promising All-Solid-State Batteries for Future Electric Vehicles. *ACS Energy Lett.* **2020**, *5* (10), 3221−3223.

(12) Zou, C.; Zang, Z.; Tao, X.; Yi, L.; Chen, X.; Zhang, X.; Yang, L.; Liu, X.; Wang, X. Stabilized Cathode/Sulfide Electrolyte Interface through Conformally Interfacial Nanocoating for All-Solid-State Batteries. *ACS Appl. Energy Mater.* **2023**, *6* (6), 3599−3607.

(13) Zhou, Y.; Li, X.; Yang, Y.; Huang, X.; Tian, B. Production of Ta-Doped $Li_7La_3Zr_2O_{12}$ Solid Electrolyte with High Critical Current Density. *ACS Appl. Energy Mater.* **2022**, *5* (11), 13817−13828.

(14) Wang, J.; Zhao, S.; Zhang, A.; Zhuo, H.; Zhang, G.; Han, F.; Zhang, Y.; Tang, L.; Yang, R.; Wang, L.; Lu, S. High Lithium-Ion Conductivity, Halide-Coated, Ni-Rich NCM Improves Cycling Stability in Sulfide All-Solid-State Batteries. *ACS Appl. Energy Mater.* **2023**, *6* (7), 3671−3681.

(15) Kato, Y.; Hori, S.; Saito, T.; Suzuki, K.; Hirayama, M.; Mitsui, A.; Yonemura, M.; Iba, H.; Kanno, R. High-Power All-Solid-State Batteries Using Sulfide Superionic Conductors. *Nat. Energy* **2016**, *1* (4), 16030.

(16) Yoon, D. H.; Park, Y. J. Electrochemical Properties of Cathode According to the Type of Sulfide Electrolyte and the Application of Surface Coating. *J. Electrochem. Sci. Technol.* **2021**, *12* (1), 126−136.

(17) Cho, J. U.; Rajagopal, R.; Yoon, D. H.; Park, Y. J.; Ryu, K. S. Control of Side Reactions Using $LiNbO_3$ Mixed/Doped Solid Electrolyte for Enhanced Sulfide-Based All-Solid-State Batteries. *Chem. Eng. J.* **2023**, *452* (P1), 138955.

(18) Deiseroth, H. J.; Kong, S. T.; Eckert, H.; Vannahme, J.; Reiner, C.; Zaiß, T.; Schlosser, M. Li_6PS_5X: A Class of Crystalline Li-Rich Solids with an Unusually High Li^+ Mobility. *Angew. Chem., Int. Ed.* **2008**, *47* (4), 755−758.

(19) Adeli, P.; Bazak, J. D.; Park, K. H.; Kochetkov, I.; Huq, A.; Goward, G. R.; Nazar, L. F. Boosting Solid-State Diffusivity and Conductivity in Lithium Superionic Argyrodites by Halide Substitution. *Angew. Chem., Int. Ed.* **2019**, *58* (26), 8681−8686.

(20) Wu, Z.; Li, X.; Zheng, C.; Fan, Z.; Zhang, W.; Huang, H.; Gan, Y.; Xia, Y.; He, X.; Tao, X.; Zhang, J. Interfaces in Sulfide Solid Electrolyte-Based All-Solid-State Lithium Batteries: Characterization, Mechanism and Strategy. *Electrochem. Energy Rev.* **2023**, *6*, 10.

(21) Auvergniot, J.; Cassel, A.; Ledeuil, J. B.; Viallet, V.; Seznec, V.; Dedryvère, R. Interface Stability of Argyrodite Li_6PS_5Cl toward $LiCoO_2$, $LiNi_{1/3}Co_{1/3}Mn_{1/3}O_2$, and $LiMn_2O_4$ in Bulk All-Solid-State Batteries. *Chem. Mater.* **2017**, *29* (9), 3883−3890.

(22) Chen, R. J.; Zhang, Y. B.; Liu, T.; Xu, B. Q.; Lin, Y. H.; Nan, C. W.; Shen, Y. Addressing the Interface Issues in All-Solid-State Bulk-Type Lithium Ion Battery via an All-Composite Approach. *ACS Appl. Mater. Interfaces* **2017**, *9* (11), 9654−9661.

(23) Koerver, R.; Aygün, I.; Leichtweiß, T.; Dietrich, C.; Zhang, W.; Binder, J. O.; Hartmann, P.; Zeier, W. G.; Janek, J. Capacity Fade in Solid-State Batteries: Interphase Formation and Chemomechanical Processes in Nickel-Rich Layered Oxide Cathodes and Lithium Thiophosphate Solid Electrolytes. *Chem. Mater.* **2017**, *29* (13), 5574−5582.

(24) Banerjee, A.; Tang, H.; Wang, X.; Cheng, J. H.; Nguyen, H.; Zhang, M.; Tan, D. H. S.; Wynn, T. A.; Wu, E. A.; Doux, J. M.; Wu, T.; Ma, L.; Sterbinsky, G. E.; D'Souza, M. S.; Ong, S. P.; Meng, Y. S. Revealing Nanoscale Solid-Solid Interfacial Phenomena for Long-Life and High-Energy All-Solid-State Batteries. *ACS Appl. Mater. Interfaces* **2019**, *11* (46), 43138−43145.

(25) Xiao, Y.; Miara, L. J.; Wang, Y.; Ceder, G. Computational Screening of Cathode Coatings for Solid-State Batteries. *Joule* **2019**, *3* (5), 1252−1275.

(26) Banerjee, A.; Wang, X.; Fang, C.; Wu, E. A.; Meng, Y. S. Interfaces and Interphases in All-Solid-State Batteries with Inorganic Solid Electrolytes. *Chem. Rev.* **2020**, *120* (14), 6878−6933.

(27) Min, K.; Seo, S. W.; Choi, B.; Park, K.; Cho, E. Computational Screening for Design of Optimal Coating Materials to Suppress Gas Evolution in Li-Ion Battery Cathodes. *ACS Appl. Mater. Interfaces* **2017**, *9* (21), 17822−17834.

(28) Xiao, Y.; Wang, Y.; Bo, S. H.; Kim, J. C.; Miara, L. J.; Ceder, G. Understanding Interface Stability in Solid-State Batteries. *Nat. Rev. Mater.* **2019**, *5*, 105−126.

(29) Yoon, D. H.; Park, Y. J. Effects of Lithium Bis(Oxalato)Borate-Derived Surface Coating Layers on the Performances of High-Ni Cathodes for All-Solid-State Batteries. *Appl. Energy* **2022**, *326*, 119991.

(30) Walther, F.; Strauss, F.; Wu, X.; Mogwitz, B.; Hertle, J.; Sann, J.; Rohnke, M.; Brezesinski, T.; Janek, J. The Working Principle of a $Li_2CO_3/LiNbO_3$ Coating on NCM for Thiophosphate-Based All-Solid-State Batteries. *Chem. Mater.* **2021**, *33* (6), 2110−2125.

(31) Ohta, N.; Takada, K.; Sakaguchi, I.; Zhang, L.; Ma, R.; Fukuda, K.; Osada, M.; Sasaki, T. $LiNbO_3$-Coated $LiCoO_2$ as Cathode Material for All Solid-State Lithium Secondary Batteries. *Electrochem. Commun.* **2007**, *9* (7), 1486−1490.

(32) Li, X.; Jin, L.; Song, D.; Zhang, H.; Shi, X.; Wang, Z.; Zhang, L.; Zhu, L. $LiNbO_3$-Coated $LiNi_{0.8}Co_{0.1}Mn_{0.1}O_2$ Cathode with High

https://doi.org/10.1021/acsomega.3c09545
ACS Omega 2024, 9, 8405−8416

Discharge Capacity and Rate Performance for All-Solid-State Lithium Battery. *J. Energy Chem.* **2020**, *40*, 39−45.
(33) Ito, S.; Fujiki, S.; Yamada, T.; Aihara, Y.; Park, Y.; Kim, T. Y.; Baek, S. W.; Lee, J. M.; Doo, S.; Machida, N. A Rocking Chair Type All-Solid-State Lithium Ion Battery Adopting Li_2O-ZrO_2 Coated $LiNi_{0.8}Co_{0.15}Al_{0.05}O_2$ and a Sulfide Based Electrolyte. *J. Power Sources* **2014**, *248*, 943−950.
(34) Strauss, F.; Teo, J. H.; Maibach, J.; Kim, A. Y.; Mazilkin, A.; Janek, J.; Brezesinski, T. Li_2ZrO_3-Coated NCM622 for Application in Inorganic Solid-State Batteries: Role of Surface Carbonates in the Cycling Performance. *ACS Appl. Mater. Interfaces* **2020**, *12* (51), 57146−57154.
(35) Payandeh, S.; Strauss, F.; Mazilkin, A.; Kondrakov, A.; Brezesinski, T. Tailoring the $LiNbO_3$ Coating of Ni-Rich Cathode Materials for Stable and High-Performance All-Solid-State Batteries. *Nano Res. Energy* **2022**, *1* (3), No. e9120016.
(36) Lim, C. B.; Park, Y. J. Precursor-Based Surface Modification of Cathodes Using Ta and W for Sulfide-Based All-Solid-State Batteries. *Sci. Rep.* **2020**, *10*, 10501.
(37) Sakuda, A.; Hayashi, A.; Tatsumisago, M. Interfacial Observation between $LiCoO_2$ Electrode and Li_2S-P_2S_5 Solid Electrolytes of All-Solid-State Lithium Secondary Batteries Using Transmission Electron Microscopy. *Chem. Mater.* **2010**, *22* (3), 949−956.
(38) Lee, J. Y.; Park, Y. J. Li_3PO_4 Coated $Li[Ni_{0.75}Co_{0.1}Mn_{0.15}]O_2$ Cathode for All-Solid-State Batteries Based on Sulfide Electrolyte. *J. Electrochem. Sci. Technol.* **2022**, *13* (3), 407−415.
(39) Lee, J. Y.; Noh, S.; Seong, J. Y.; Lee, S.; Park, Y. J. Suppressing Unfavorable Interfacial Reactions Using Polyanionic Oxides as Efficient Buffer Layers: Low-Cost Li_3PO_4 Coatings for Sulfide-Electrolyte-Based All-Solid-State Batteries. *ACS Appl. Mater. Interfaces* **2023**, *15* (10), 12998−13011.
(40) Kaneda, H.; Koshika, Y.; Nakamura, T.; Nagata, H.; Ushio, R.; Mori, K. Improving the Cycling Performance and Thermal Stability of $LiNi_{0.6}Co_{0.2}Mn_{0.2}O_2$ Cathode Materials by Nb-doping and Surface Modification. *Int. J. Electrochem. Sci.* **2017**, *12* (6), 4640−4653.
(41) Lei, Y.; Ai, J.; Yang, S.; Lai, C.; Xu, Q. Nb-doping in $LiNi_{0.8}Co_{0.1}Mn_{0.1}O_2$ Cathode Material: Effect on the Cycling Stability and Voltage Decay at High Rates. *J. Taiwan Inst. Chem. Eng.* **2019**, *97*, 255−263.
(42) Li, Z.; Hu, G.; Luo, Z.; Huang, M.; Zhang, S.; Du, K.; Peng, Z.; Tan, X.; Zhao, W.; Yan, Q.; Cao, Y. Ta Doping and $LiTaO_3$ Coating to Improve the Electrochemical Performance of $LiNi_{0.925}Co_{0.03}Mn_{0.045}O_2$ Cathode Material for Lithium Ion Batteries. *Solid State Ionics* **2023**, *394*, 116190.
(43) Sun, H. H.; Kim, U. H.; Park, J. H.; Park, S. W.; Seo, D. H.; Heller, A.; Mullins, C. B.; Yoon, C. S.; Sun, Y. K. Transition Metal-doped Ni-rich Layered Cathode Materials for Durable Li-ion Batteries. *Nat. Commun.* **2021**, *12*, 6552.
(44) Tang, Y.; Han, X.; Zhang, W.; He, Y. La Doping and Coating Enabled by One-step Method for High Performance $Li_{1.2}Mn_{0.54}Ni_{0.13}Co_{0.13}O_{0.2}$ Li-rich Cathode. *Ionics* **2020**, *26*, 3737−3747.
(45) Zheng, H. W.; Liu, Z. C.; Chen, Y. Z.; Gao, X. P. La-Doped Ultrahigh-Nickel Layered Oxide Cathode with Enhanced Cycle Stability for Li-Ion Batteries. *ACS Appl. Mater. Interfaces* **2023**, *15* (29), 35043−35051.
(46) Kim, A. Y.; Strauss, F.; Bartsch, T.; Teo, J. H.; Hatsukade, T.; Mazilkin, A.; Janek, J.; Hartmann, P.; Brezesinski, T. Stabilizing Effect of a Hybrid Surface Coating on a Ni-Rich NCM Cathode Material in All-Solid-State Batteries. *Chem. Mater.* **2019**, *31* (23), 9664−9672.
(47) Vadhva, P.; Hu, J.; Johnson, M. J.; Stocker, R.; Braglia, M.; Brett, D. J. L.; Rettie, A. J. E. Electrochemical Impedance Spectroscopy for All-Solid-State Batteries: Theory, Methods and Future Outlook. *ChemElectroChem.* **2021**, *8* (11), 1930−1947.
(48) Morino, Y. Impact of Surface Coating on the Low Temperature Performance of a Sulfide-Based All-Solid-State Battery Cathode. *Electrochemistry* **2022**, *90* (2), 027001.
(49) Fukunishi, G.; Tabuchi, M.; Ikezawa, A.; Okajima, T.; Kitamura, F.; Suzuki, K.; Hirayama, M.; Kanno, R.; Arai, H. AC Impedance Analysis of NCM523 Composite Electrodes in All-Solid-State Three Electrode Cells and Their Degradation Behavior. *J. Power Sources* **2023**, *564* (30), 232864.
(50) Togasaki, N.; Nakao, A.; Tanaka, T.; Harada, U.; Onish, H.; Yasuda, H.; Kobayashi, S.; Maeda, F.; Osaka, T. Utilization Ratio of Active Materials in All-Solid-State Batteries Examined Using Electrochemical Impedance Analysis with the Transmission Line Model. *J. Electrochem. Soc.* **2023**, *170* (5), 050519.
(51) Morino, Y.; Sano, H.; Kawaguchi, S.; Hori, S.; Sakuda, A.; Takahashi, T.; Miyashita, N.; Hayashi, A.; Kanno, R. High-Frequency Impedance Spectroscopic Analysis of Argyrodite-Type Sulfide-Based Solid Electrolyte upon Air Exposure. *J. Phys. Chem. C* **2023**, *127* (37), 18678−18683.
(52) Lee, J. S.; Park, Y. J. Comparison of $LiTaO_3$ and $LiNbO_3$ Surface Layers Prepared by Post- And Precursor-Based Coating Methods for Ni-Rich Cathodes of All-Solid-State Batteries. *ACS Appl. Mater. Interfaces* **2021**, *13* (32), 38333−38345.
(53) Morino, Y. Degradation Rate at the Solid-Solid Interface of Sulfide-Based Solid Electrolyte-Cathode Active Material. *J. Powder Sources* **2022**, *541* (1), 231672.
(54) Tan, D. H. S.; Chen, Y. T.; Yang, H.; Bao, W.; Sreenarayanan, B.; Doux, J. M.; Li, W.; Lu, B.; Ham, S. Y.; Sayahpour, B.; Scharf, J.; Wu, E. A.; Deysher, G.; Han, H. E.; Hah, H. J.; Jeong, H.; Lee, J. B.; Chen, Z.; Meng, Y. S. Carbon-Free High-Loading Silicon Anodes Enabled by Sulfide Solid Electrolytes. *Science* **2021**, *373* (6562), 1494−1499.
(55) Walther, F.; Koerver, R.; Fuchs, T.; Ohno, S.; Sann, J.; Rohnke, M.; Zeier, W. G.; Janek, J. Visualization of the Interfacial Decomposition of Composite Cathodes in Argyrodite-Based All-Solid-State Batteries Using Time-of-Flight Secondary-Ion Mass Spectrometry. *Chem. Mater.* **2019**, *31* (10), 3745−3755.
(56) Riphaus, N.; Stiaszny, B.; Beyer, H.; Indris, S.; Gasteiger, H. A.; Sedlmaier, S. J. Editors' Choice—Understanding Chemical Stability Issues between Different Solid Electrolytes in All-Solid-State Batteries. *J. Electrochem. Soc.* **2019**, *166* (6), A975−A983.
(57) Kato, A.; Kowada, H.; Deguchi, M.; Hotehama, C.; Hayashi, A.; Tatsumisago, M. XPS and SEM Analysis between Li/Li_3PS_4 Interface with Au Thin Film for All-Solid-State Lithium Batteries. *Solid State Ionics* **2018**, *322*, 1−4.

https://doi.org/10.1021/acsomega.3c09545
ACS Omega 2024, 9, 8405−8416